OPTICS

Miniaturizing color-sensitive photodetectors via hybrid nanoantennas toward submicrometer dimensions

Jinfa Ho[1] †, Zhaogang Dong[1,2*†], Hai Sheng Leong[1], Jun Zhang[1], Febiana Tjiptoharsono[1], Soroosh Daqiqeh Rezaei[3], Ken Choon Hwa Goh[1], Mengfei Wu[1], Shiqiang Li[1], Jingyee Chee[1], Calvin Pei Yu Wong[1], Arseniy I. Kuznetsov[1], Joel K. W. Yang[1,3*]

Digital camera sensors use color filters on photodiodes to achieve color selectivity. As the color filters and photosensitive silicon layers are separate elements, these sensors suffer from optical cross-talk, which sets limits to the minimum pixel size. Here, we report hybrid silicon-aluminum nanostructures in the extreme limit of zero distance between color filters and sensors. This design could essentially achieve submicrometer pixel dimensions and minimize the optical cross-talk arising from tilt illuminations. The designed hybrid silicon-aluminum nanostructure has dual functionalities. Crucially, it supports a hybrid Mie-plasmon resonance of magnetic dipole to achieve color-selective light absorption, generating electron hole pairs. Simultaneously, the silicon-aluminum interface forms a Schottky barrier for charge separation and photodetection. This design potentially replaces the traditional dye-based filters for camera sensors at ultrahigh pixel densities with advanced functionalities in sensing polarization and directionality, and UV selectivity via interband plasmons of silicon.

INTRODUCTION

Miniaturization of complementary metal oxide semiconductor (CMOS) color sensors based on silicon (Si) technology could enable high-resolution light-field sensor arrays (*1*), hyperspectral imaging (*2*), and miniaturized spectrometers (*3*–*5*). However, due to its broadband absorption in the visible spectrum, Si-based photodetectors are intrinsically "color blind." Thus, color filters are layered onto the detectors to achieve spectral sensitivity. Typical color filters consist of conventional dye-based red-green-blue (RGB) color filters, linear variable filters (*6*–*8*), and Fabry-Perot etalon bandpass filters (*9*, *10*). However, an inherent drawback in these approaches is the optical cross-talk that occurs when sensors are juxtaposed. Cross-talk occurs when light passing through one color filter is undesirably absorbed by surrounding photodetector elements. Although this problem can be partially mitigated via back-side illumination detector technology that decreases the distance between color filters and the light-absorbing Si layer beneath, parallax effects limit the degree of miniaturization of optical detectors to dimensions larger than a few micrometers.

Recently, various designs to miniaturize spectrally selective photodetectors have used nanowires (*3*, *11*–*15*), large array filters (*2*, *4*, *16*–*18*), plasmonic hot electrons (*19*–*26*), graphene nanoribbons (*27*, *28*), colloidal quantum dot absorption (*29*), photonic crystals (*30*, *31*), Schottky barrier for near-infrared (IR) regime (*19*, *20*), and indium tin oxide–Si junction with scanning probe setup (*32*). However, these approaches are ill suited for scale-up and/or incompatible with CMOS fabrication processes. On the other hand, other approaches based on tall Si nanowires, incorporating *p-i-n* junctions (*5*, *33*), achieve miniaturized spectrometer functionalities due to waveguide mode resonances. Nevertheless, this approach is generally limited in scalability and miniaturization. Alternatively, other CMOS compatible color sensor designs are based on *p-i-n* anti-Hermitian Si metasurface (*34*) or the aluminum (Al)–Si junction with a large pixel size of ~10 μm (*21*). In addition, both designs (*21*, *34*) exhibit substantial dark current, which induces a large background signal for photodetection.

Here, we explore the extreme limit of decreasing the separation between color filter and sensor to zero, by nanopatterning a light-absorbing Si-Al layer that directly imparts color sensitivity to Si. This design could essentially push pixel dimensions to the submicrometer regime and minimize cross-talks between adjacent color channels, originating from tilt illuminations. The hybrid Si-Al nanostructures support a hybrid plasmon-Mie resonance to achieve intrinsic color sensitivity. Magnetic resonances (*35*–*37*) and low optical losses make high-index semiconductors, such as Si, particularly attractive for applications in wavelength selective photodetection. Magnetic resonances exhibit field confinement within the dielectric nanostructures. Thus, it effectively increases the optical path within Si to promote photocurrent generation. Sharp spectral resonances in subwavelength Si nanodisks have been demonstrated because of low optical losses, indicating their suitability as miniaturized spectral filters. Crucially, Si devices and nanofabrication processes are mature, allowing for solutions based on Si nanostructures to be easily scaled up and implemented in commercial products, with prospects toward full ultraviolet (UV)–visible multispectral photometers leveraging on interband plasmonic characteristics of Si nanostructures in the UV (*38*).

RESULTS

Design of the color-sensitive detectors with hybrid Mie-plasmon resonance

Figure 1A presents the schematic illustration of the color-sensitive detector, which consists of Si nanoposts with Al disks on top and Al

[1]Institute of Materials Research and Engineering, A*STAR (Agency for Science, Technology and Research), 2 Fusionopolis Way, #08-03 Innovis, 138634 Singapore, Singapore. [2]Department of Materials Science and Engineering, National University of Singapore, 9 Engineering Drive 1, 117575 Singapore, Singapore. [3]Singapore University of Technology and Design, 8 Somapah Road, 487372 Singapore, Singapore. *Corresponding author. Email: joel_yang@sutd.edu.sg (J.K.W.Y.); dongz@imre.a-star.edu.sg (Z.D.)
†These authors contributed equally to this work.

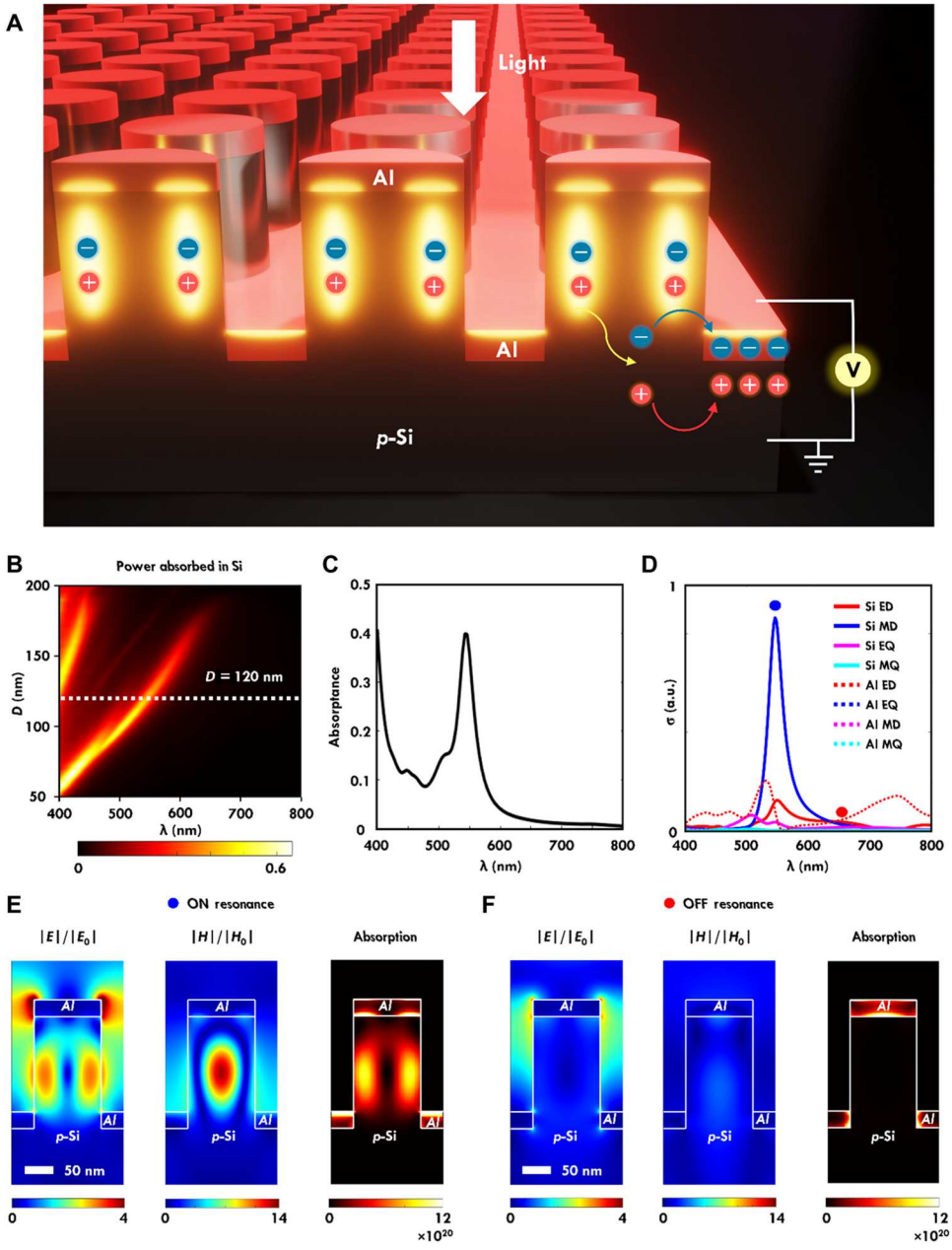

Fig. 1. Design of the color-sensitive optical detectors based on the hybrid *p*-Si and Al nanostructures. (**A**) Schematic illustration of the designed color-sensitive detector. The designed device array has a fixed pitch size Λ of 200 nm and a height *h* of 200 nm, with 30-nm-thick Al film. (**B**) Simulated optical absorptance spectra when the Si nanodisk diameter *D* is varied from 50 to 200 nm. Higher-order absorption peaks appear for nanodisks with diameters larger than 125 nm. (**C**) Absorptance spectrum for nanodisk array with a diameter *D* = 120 nm in Si. (**D**) Multipolar decomposition of the scattering cross section (σ) showing contributions of the ED, MD, EQ, and MQ supported by the hybrid Si-Al nanodisk array (*D* = 120 nm), highlighting dominant resonance due to MD in Si. a.u., arbitrary units. (**E**) Spatial distributions of electric field |***E***| and magnetic field |***H***| at the resonance wavelength of ~540 nm, corresponding to the absorption of Si MD peak for *D* = 120 nm. The absorption plot shows that absorption happens mostly within the *p*-Si nanostructures to generate electron-hole pairs. (**F**) Spatial distributions of electric field |***E***| and magnetic field |***H***| at an off-resonance wavelength of 650 nm for *D* = 120 nm.

film between the posts. We chose *p*-Si as the substrate as it is widely used in the semiconductor industry. The refractive index of *p*-Si is shown in fig. S1. On the other hand, Al is suitable because it forms a sub-1-eV Schottky barrier with *p*-Si, is CMOS compatible, and supports plasmon resonances. Using finite-difference time-domain (FDTD) simulations, we obtained a suitable design consisting of nanodisk arrays with a height *h* of 200 nm and a pitch Λ of 200 nm, used throughout the article. The diameter *D* of the Si nanodisk array is varied to achieve the desired color sensitivity for red, green, and blue. A 30-nm Al layer was then deposited using electron beam evaporation. This layer has the following functionalities: The Al disk on Si nanostructure functions as a hybrid plasmon-Mie resonator,

enabling enhanced absorption at the selected light wavelength. Simultaneously, the Al film forms a Schottky barrier with the *p*-doped Si substrate as the holes from the *p*-Si region diffuse toward Al to equilibrate Fermi levels. As a result, Al film is positively charged, and the *p*-Si region is negatively charged with a depletion region formed (see the detailed illustration in fig. S2). Therefore, because of these two functionalities, this Si-Al nanostructure can function as a nanoscopic color-sensitive photodiode with size-tunable spectral selectivity.

Because of the rotational symmetry of nanodisks, the photoresponse is independent of the incident light polarization. Nevertheless, introducing polarization dependence to the photodetectors by symmetry breaking would be straightforward (*39*–*41*). FDTD simulations were performed to investigate the absorption characteristic inside Si region as a function of nanodisk diameter, as shown in Fig. 1B. Strong size-dependent absorption peaks could be engineered to achieve color sensitivity, in stark contrast to the intrinsic material absorption of Si, which monotonically decreases from 400 to 800 nm (*42*, *43*). In addition, Fig. 1B shows that the fundamental absorption peak is observed at ~400 nm for the nanodisk diameter D = 50 nm and red shifts to ~625 nm when D increases to 170 nm. Similarly, the absorption peak due to higher-order mode is also observed for larger nanodisks, appearing at 400 nm for nanodisk diameter D = 130 nm and red shifting to ~440 nm for D = 190 nm. For comparison, Fig. 1C and fig. S3 present the absorption characteristics of Si nanodisk with and without Al film, respectively, where a sharper response of absorption spectrum is obtained with Al film. The sharper absorption is due to the enhanced magnetic dipole (MD) in Si by the electric dipole (ED) of the Al nanodisk on top. In addition, fig. S4 presents the absorption characteristics of the pure plasmonic resonance of Al nanostructures.

To elucidate the nature of the absorption peaks, we show multipolar decomposition results in Fig. 1D. It presents the relative scattering cross sections of the ED, electric quadrupole (EQ), MD, and magnetic quadrupoles (MQs) of the Si-Al nanostructure, for D = 120 nm. Clearly, enhanced absorption is attributed to the MD resonance in the Si nanodisk, with corresponding electric field $|\boldsymbol{E}|$ and magnetic field $|\boldsymbol{H}|$ distributions shown in Fig. 1E, where the corresponding vectorial electric field and plasmon charge distribution are shown in fig. S5. The enhanced electric field around the Al nanodisk is due to the excitation of localized plasmon resonances (*41*). The electric field is also highly confined within the Si nanodisk, where it leads to photon absorption and electron-hole pair generation. These generated electron-hole pairs will be charge separated first due to the internal built-in electrical field, and then, they diffuse a short distance to be collected by the respective electrodes, such as Al metal at the base of the Si pillars, where the Al film is electrically connected to external electronics. As shown in Fig. 1E, the distance between the peak absorption location inside *p*-Si nanodisks and the Al film is only ~70 nm, where this distance is much smaller than the typical diffusion length of ~100 μm in Si.

On the other hand, the Al film on top of the Si nanodisk is electrically isolated; however, a charge depletion region still forms (see the detailed schematic illustration on this junction creation process in fig. S2). In comparison, Fig. 1F presents the corresponding electric field $|\boldsymbol{E}|$ and magnetic field $|\boldsymbol{H}|$ distribution off-resonance (i.e., λ = 650 nm). It shows that the electrical fields predominantly lie outside the Si nanostructures, leading to minimal light absorption or photocurrent generation. Similar analysis for a larger nanodisk with d = 150 nm shows a more complex field distribution within the nanostructure as the resonant wavelength red shifts to ~600 nm, as shown in fig. S6.

Fabrication and characterization

To fabricate the samples, we exposed nanodisk patterns using electron beam lithography in hydrogen silsesquioxane (HSQ) resist that was spin-coated on *p*-type prime grade <100> Si wafers (Si Valley Microelectronics Inc., resistivity of 10 to 50 ohm·cm). Samples were then etched using inductively coupled plasma (ICP) to form Si nanodisk arrays (*44*) (see details in Materials and Methods). The thickness of HSQ resist is optimized such that HSQ mask is etched away completely when the dry etching is done. After the etching process, 30-nm-thick Al film was then evaporated onto the sample to work as the top electrode via electron beam evaporation, to form a reliable Si-Al Schottky junction. We observed that hydrofluoric treatment should not be performed on these Si nanostructures, as it probably introduces surface states that produce ohmic-like contact between Si and Al (see fig. S7 for details).

Figure 2A presents a scanning electron microscopy (SEM) image of the Si-Al nanoantenna with a diameter D of 120 nm. The corresponding angle-resolved reflectance spectrum in the back focal plane is shown in Fig. 2B, and Fig. 2C presents the reflectance spectra at the respective incident angles of 0°, 15°, and 30°. To characterize the Schottky barrier photodiode, the diode is reverse-biased as shown in Fig. 2D, where a positive voltage is applied to the top Al electrode with the Si back contact set to ground. Figure 2E presents the measured *I*-*V* curves, which were obtained from a Keithley 2450 sourcemeter with and without laser illumination. The corresponding *I*-*V* curves at linear scale are shown in fig. S8A, showing a dark current of ~52 nA at a reverse bias voltage of 0.5 V.

The electrical characteristics of the nanostructured Al-Si Schottky device can be modeled using equations for thermionic emission (*45*, *46*)

$$I = AA^{**}T^2 \exp\left(-\frac{q\phi}{kT}\right)\left[\exp\left(\frac{qV}{nkT}\right) - 1\right] \quad (1)$$

where q denotes the fundamental charge of an electron, T is the device temperature, k is the Boltzmann constant, A is the device electrode area of ~0.07 cm^2, and A^{**} denotes the Richardson constant of *p*-Si = 32 A cm^{-2} K^{-2}. When fitting the *I*-*V* curve in the linear range of 0.04 to 0.10 V based on Eq. 1, the Schottky barrier height ϕ of the device is estimated to be ~0.816 eV with an ideality factor n of ~1.09.

In addition, the depletion width W of the Schottky barrier is estimated using

$$W = \sqrt{\frac{2\epsilon_s}{qN_A}\left(V_{Bi} - V - \frac{kT}{q}\right)} \quad (2)$$

where V_{Bi} denotes the built-in potential being the difference between the Schottky barrier height and the Fermi level of the semiconductor. V_{Bi} has a value of 0.587 V, based on the exacted Schottky barrier height ϕ of ~0.816 eV (*47*). ϵ_s denotes the relative permittivity and ϵ_s = 11.68 (*46*). N_A denotes the doping concentration of *p*-Si, with a value of ~1.38×10^{15} cm^{-3}. V denotes the externally applied potential. The depletion width W is calculated to be ~700 nm at 0

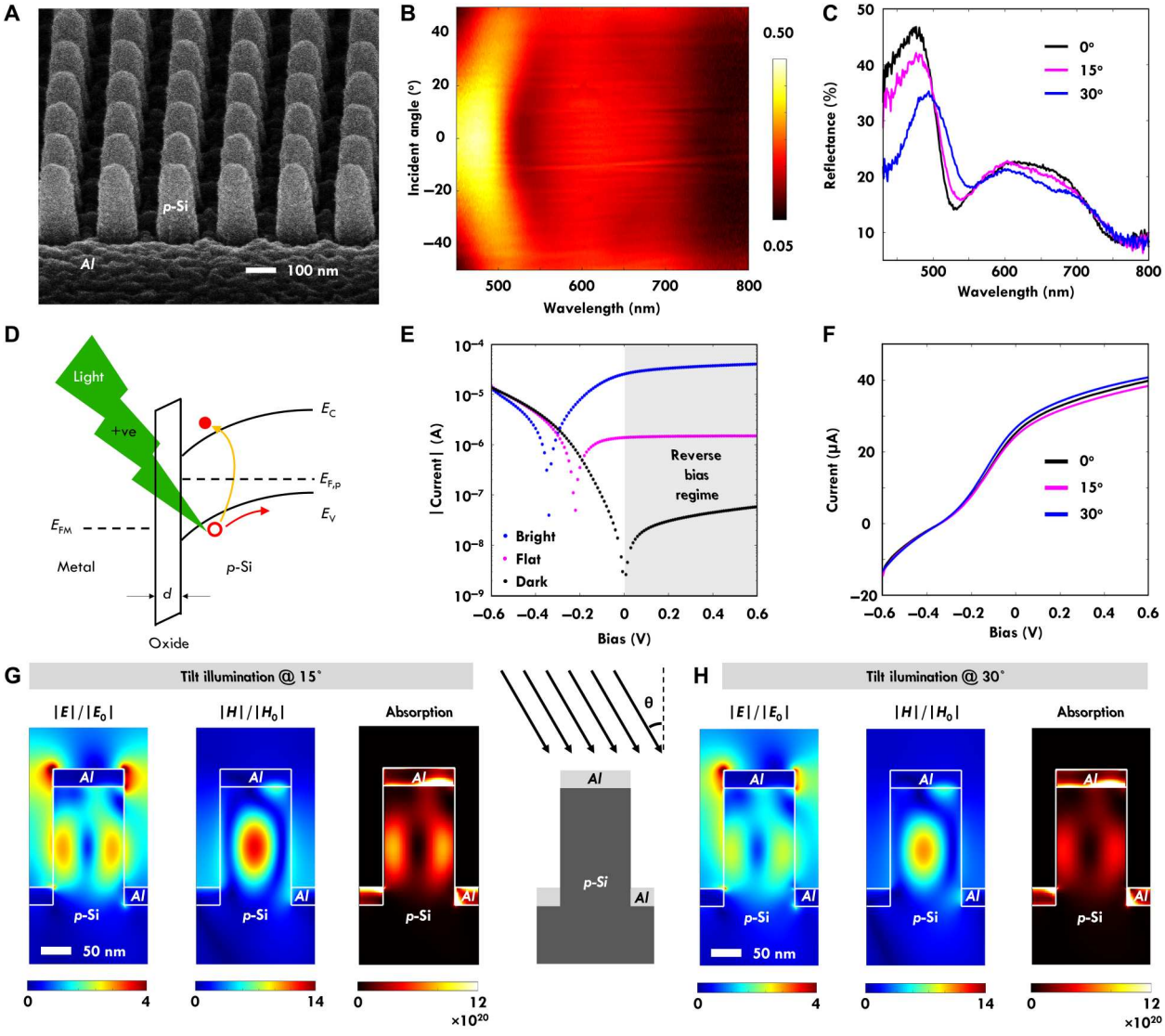

Fig. 2. Characterization results of the fabricated color-sensitive detector devices. (**A**) SEM image of a sample patterned with nanodisks with diameter *D* of ~120 nm, a pitch of 200 nm, and a height of 200 nm. (**B**) Angle-resolved reflectance spectra as measured in the back focal plane showing minimal incident angle dependence. (**C**) Measured reflectance spectra at the respective incident angles of 0°, 15°, and 30°. (**D**) Energy band diagram of the device under reverse bias condition, which widens the depletion region and facilitates charge separation. Electron-hole pairs are generated in the depletion region, followed by charge separation with holes (electrons) moving to the right (left) into *p*-Si semiconductor (metal contact), resulting in a larger positive current under reverse bias. The thickness *d* of the native silicon oxide is ~2 nm based on ellipsometer measurement. (**E**) *I-V* characterization result of the nanostructured device at logarithmic scale under "dark" and "bright" illumination conditions. The observed *I-V* curves correspond to a typical Schottky barrier photodiode device, where photocurrent is clearly observed under reverse bias condition (i.e., a positive voltage being applied to the top Al electrode and Si back contact set to ground). The incident light source is a 532-nm laser with a laser power of 0.78 mW, where the photocurrent measured from the flat unpatterned region is shown for comparison. (**F**) Photocurrent measurement of the detector element with the respective tilt angles of 0°, 15°, and 30°. It shows that the photocurrent from the nanostructured color detector does not change significantly with respect to the tilted light illuminations. (**G** and **H**) Simulated absorption profiles when the laser illumination has the respective tilt angles of 15° and 30°. The tilted light illumination configuration is shown in (G).

bias, suggesting that the *p*-Si nanostructures are completely depleted.

The measured responsivity of the nanostructured detector element is 47.2 mA/W, corresponding to an external quantum efficiency of ~9%, where the efficiency of the proposed photodetector and other Si photodetectors in the literature is compared with details shown in table S1. At this bias condition and with 0.78 mW of 532-nm laser illumination, the photocurrent was ~800-fold higher than the dark current. Moreover, the photocurrent was ~31-fold higher with laser illuminating the patterned array compared to the flat region, as shown in Fig. 2E. In addition, Fig. 2F presents photocurrent measurement of the detector element with the respective tilt angles of 0°, 15°, and 30°. It shows that the photocurrent from the nanostructured color detector does not change significantly with respect to the incident angle, corroborated with simulated absorption profiles for incident angles of 15° and 30° in Fig. 2 (G and H) that look similar to that of normal incidence. In other words, the optical antenna effects of the hybrid Si-

Al nanostructures appear to behave similarly to microlenses, which are able to collect the light even for inclined illuminations.

To characterize the wavelength-dependent photoresponse of the nanodisks systematically, we tested 32 nanodisk arrays with a constant period of 200 nm, and the diameter *D* varied from 10 to 200 nm in steps of ~5.4 nm, as indicated in the optical micrograph in Fig. 3A. The nanodisk arrays with diameter *D* less than 50 nm are not fully fabricated because some of these nanodisks with small diameters do not have sufficient adhesion to the substrate during the resist development process. For optical characterization, we raster-scanned continuous wave lasers with wavelengths of 488 nm (blue), 532 nm (green), and 633 nm (red) over the device and recorded the photocurrent at each position of the sample. The device was reverse-biased at 0.5 V, and the intensity of the lasers was kept at 0.3 mW. Figure 3B shows the normalized photocurrent maps of the arrays, and the wavelength-dependent photoresponse is clearly observed as the arrays with larger nanodisk diameters have higher photocurrent as the wavelength is increased. Good agreement was observed between the experimentally measured photocurrent and the simulated absorption of the Si region, as shown in Fig. 3C.

Next, we reduced the dimensions of these detector devices from 10 μm × 10 μm, down to 5 μm × 5 μm and 1 μm × 1 μm. Figure 4A shows the spectral response of three representative arrays sensitive to red, green, and blue. These device arrays consist of 36 color-sensitive photodetector devices, where the nanodisk arrays have a height of 200 nm, a fixed period of 200 nm, and a varying diameter *D* from 10 to 200 nm. Generally, the peak resonance wavelength is red shifted with increasing disk diameter. Figure 4B presents the SEM images of the typical nanodisk arrays with an area of 1 μm × 1 μm, while the SEM images of the typical nanodisk arrays with an area of 5 μm × 5 μm are shown in fig. S9. The corresponding photocurrent responses (dots) from the devices as measured experimentally are shown in Fig. 4C. These measurement results are benchmarked with simulation (solid curves), showing a good agreement. Note that the photocurrent maps at 633 nm in Figs. 3B and 4A appear noisier compared to two other wavelengths due to the lower light absorption efficiency at 633 nm (see detailed simulation analysis at fig. S10). In addition, the developed color-sensitive photodetectors were also characterized using white light illumination as shown in fig. S11.

DISCUSSION

The miniaturized color-sensitive detectors could potentially be integrated within a single-element design as shown in fig. S12, where each detector has the accompanying electronics with a couple of transistors connected to it, similar to the current CMOS sensors. In addition, this color-sensitive photodetector can be extended to

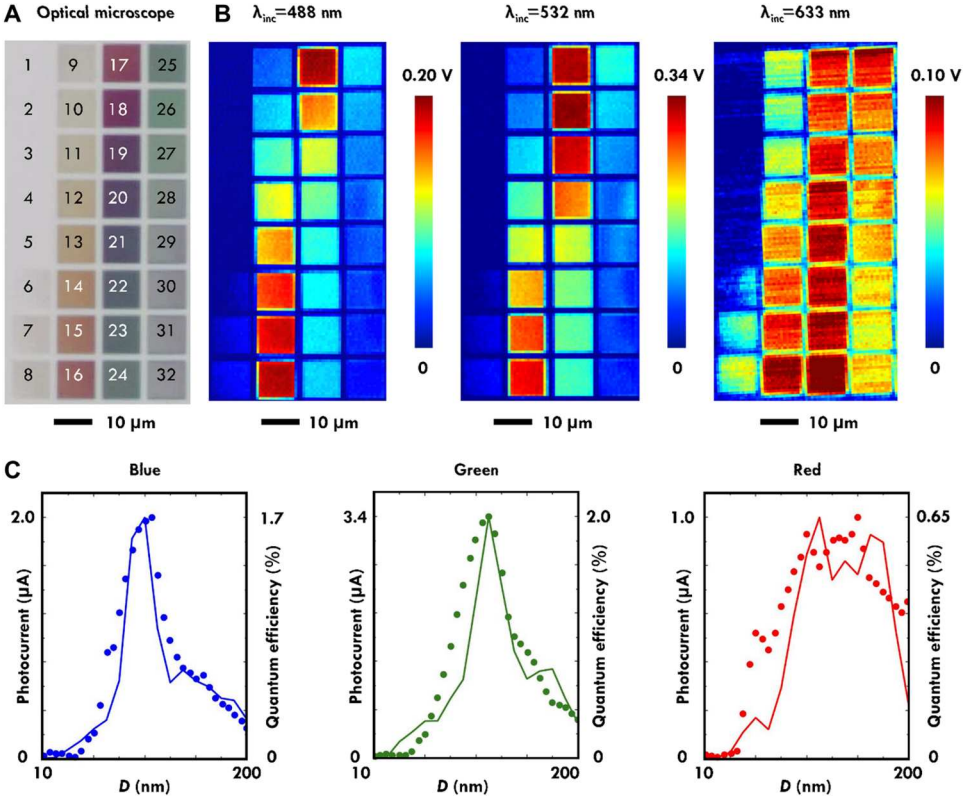

Fig. 3. Optical and photocurrent measurements at red, green, and blue wavelengths for arrays of Si-Al hybrid structures. (**A**) Optical microscope reflection image of the device. It consists of 32 color-sensitive photodetector arrays with diameter *D* ranging from 10 to 200 nm. Each photodetector array has an area of 10 μm × 10 μm. (**B**) Normalized photocurrent maps of the device under the illumination laser with the respective wavelengths of 488 nm (left), 532 nm (middle), and 633 nm (right). The device was reversed-biased at 0.5 V. Note that the photocurrent mapping in (B) was obtained by raster scanning a focused laser spot across the sample and measuring the photocurrent at each point and converting it to a voltage in the map, as the gain of the *I-V* amplifier was 10^5 V/A. (**C**) Comparison of the experimentally observed photocurrent (dots) with simulated absorption in Si (solid curves), showing good agreement. The simulation was carried out with 50 × 50 nanodisks.

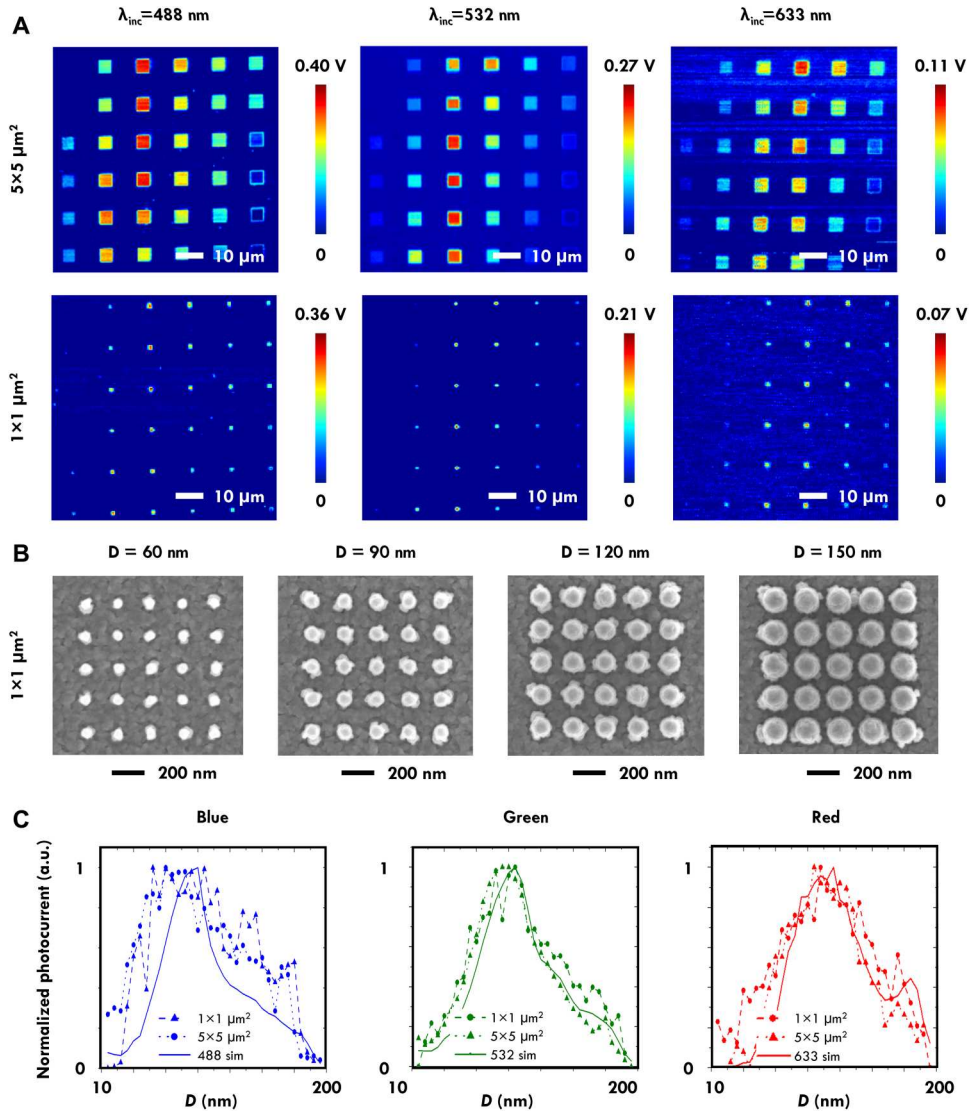

Fig. 4. Miniaturizing the color-sensitive detector devices down to 1 μm × 1 μm. (**A**) Normalized photocurrent maps of the device under 488-nm (left), 532-nm (middle), and 633-nm (right) laser illumination for the detector devices with the respective dimensions of 5 μm × 5 μm and 1 μm × 1 μm. The device consists of 36 color-sensitive photodetector arrays and was reverse-biased at 0.5 V. The gain of the photocurrent *I-V* amplifier was set to 10^5 V/A. The nanodisk diameters were varied nominally from 10 to 200 nm in these devices, where the nanodisk height is 200 nm and the pitch size is fixed at 200 nm. (**B**) SEM images of the typical nanodisk array with the area of 1 μm × 1 μm. (**C**) Experimentally measured photocurrent response (dots) from the devices with the area of 1 μm × 1 μm and 5 μm × 5 μm, in comparison with simulation result (solid curves), showing a good agreement. The simulation was carried out with 5 × 5 nanodisks.

achieve polarization sensitivity via asymmetric nanostructures, such as ellipses or dimers (*40*). Moreover, the spectral range of our current detector design could be potentially extended into the UV regime by leverating on the interband plasmonic property ofSi (*38*). This color detector configuration lends itself conveniently to realize miniaturized spectrometers that could reconstruct an arbitrary input spectrum through photocurrent responses via algorithmic means. At ultrahigh pixel densities, cross-talk due to charge spreading between different pixels could be problematic, but CMOS solutions are readily available, e.g., charge barrier structures in the form of deep trenches between pixels (*48*).

Here, we have designed and fabricated color-sensitive hybrid Si-Al photodetectors with a small pixel dimension of 1 μm × 1 μm. This hybrid Si-Al nanostructure performs two functionalities simultaneously. Optically, it supports the hybrid Mie-plasmon resonance, especially the MD component, to achieve the spectrally selective absorption of light, which leads to the excitation of electron-hole pairs. Electronically, this hybrid Si-Al nanostructure crucially forms a Schottky barrier, to separate the generated electron-hole pairs for photodetection. The technology developed here could potentially be further optimized to replace the traditional dye-based CMOS camera filters for easier fabrication of camera sensors at higher pixel densities and extending the broadband detection range to the UV regime (*38*).

MATERIALS AND METHODS

Fabrication of Si nanoantenna array

HSQ etching mask was first fabricated on the single-crystalline *p*-doped Si (resistivity = 10 to 50 ohm·cm, prime grade; Si Valley Microelectronics Inc.). HSQ resist (Dow Corning, XR-1541-006) was first diluted to 3% using methyl isobutyl ketone solvent and spin-coated onto a cleaned substrate at 3000 rpm to obtain an HSQ thickness of ~50 nm. Electron beam exposure was then carried out with an electron acceleration voltage of 100 keV (EBL, Elionix ELS-7000), a beam current of 500 pA, and an exposure dose of ~12 mC/cm^2. The sample was then developed by NaOH/NaCl salty solution (1 wt %/4 wt % in deionized water) for 60 s and then immersed in deionized water for 60 s to stop the development. The sample was immediately rinsed with acetone and isopropanol alcohol and dried with a continuous nitrogen gas flow. Si etching of 200 nm was then carried out by ICP (Oxford Instruments, Plasmalab System 100) (*49*), with a radio frequency power of 100 W, ICP power of 150 W, Cl_2 with a flow rate of 22 sccm (standard cubic centimeter per minute), under a process pressure of 5 mtorr, and temperature of 40°C.

Scanning electron microscope

SEM images were taken at an acceleration voltage of 1 keV (Hitachi, SU8220).

Optical and electrical characterizations

Keithley 2450 source meter was used to obtain the *I*-*V* characteristics. The electrode on the surface of the sample that has the nanoantenna arrays is connected to the high potential terminal, "Force-Hi," of the source meter, while the back surface of the sample is connected to the low potential terminal, "Force-Lo." Before connecting the sample to the source meter, the back surface of the sample is lightly scraped to remove the native oxide layer. For the photocurrent measurements, our light source is a supercontinuum laser (i.e., NKT Photonics, SuperK Compact), which emits a broad spectrum ranging from 400 to 2400 nm. The output of the supercontinuum laser is then passed through a monochromator (i.e., NKT Photonics, SuperK VARIA), which can select the wavelength from 430 to 680 nm with a step size of 10 nm. The monochromatic light is then focused onto the nanoantenna array device with a 50× objective lens that has a numerical aperture of 0.50. For each wavelength, the photocurrent generated by the nanoantenna array is measured with the Keithley 2450 source meter. During the photocurrent measurements, the nanoantenna array is reverse-biased at 0.50 V and the photocurrent is converted into a voltage output via an *I*-*V* amplifier (FEMTO DLPCA-200) with a gain of 10^5 V/A. This voltage output is recorded by a data acquisition card on a Witec system (model number Alpha 300s), where the detailed schematic of this experimental setup is shown in fig. S13. The detailed formula for calculating the external quantum efficiency and responsivity is shown in the Supplementary Text.

Numerical simulations

FDTD simulations of the reflectance spectra and electric field distribution were carried out using Lumerical FDTD Solutions. Periodic boundary conditions were used, with the incident optical field being linearly polarized and at different incident angles. In addition, the details of multipolar decomposition could be found in (*50*, *51*).

Supplementary Materials

This PDF file includes:

Supplementary Text
Figs. S1 to S13
Table S1
References

REFERENCES AND NOTES

1. X. Feng, L. Gao, Ultrafast light field tomography for snapshot transient and non-line-of-sight imaging. *Nat. Commun.* **12**, 2179 (2021).
2. F. Yesilkoy, E. R. Arvelo, Y. Jahani, M. Liu, A. Tittl, V. Cevher, Y. Kivshar, H. Altug, Ultrasensitive hyperspectral imaging and biodetection enabled by dielectric metasurfaces. *Nat. Photon.* **13**, 390–396 (2019).
3. Z. Yang, T. Albrow-Owen, H. Cui, J. Alexander-Webber, F. Gu, X. Wang, T.-C. Wu, M. Zhuge, C. Williams, P. Wang, A. V. Zayats, W. Cai, L. Dai, S. Hofmann, M. Overend, L. Tong, Q. Yang, Z. Sun, T. Hasan, Single-nanowire spectrometers. *Science* **365**, 1017–1020 (2019).
4. J. J. Cadusch, J. Meng, B. Craig, K. B. Crozier, Silicon microspectrometer chip based on nanostructured fishnet photodetectors with tailored responsivities and machine learning. *Optica* **6**, 1171–1177 (2019).
5. J. Meng, J. J. Cadusch, K. B. Crozier, Detector-only spectrometer based on structurally colored silicon nanowires and a reconstruction algorithm. *Nano Lett.* **20**, 320–328 (2020).
6. A. Emadi, H. Wu, G. de Graaf, R. Wolffenbuttel, Design and implementation of a sub-nm resolution microspectrometer based on a linear-variable optical filter. *Opt. Express* **20**, 489–507 (2012).
7. A. Emadi, H. Wu, G. de Graaf, P. Enoksson, J. H. Correia, R. Wolffenbuttel, Linear variable optical filter-based ultraviolet microspectrometer. *Appl. Optics* **51**, 4308–4315 (2012).
8. P. Ji, C.-S. Park, S. Gao, S.-S. Lee, D.-Y. Choi, Angle-tolerant linear variable color filter based on a tapered etalon. *Opt. Express* **25**, 2153–2161 (2017).
9. T. Wipiejewski, K. Panzlaff, K. J. Ebeling, Resonant wavelength selective photodetectors. *Microelectron. Eng.* **19**, 223–226 (1992).
10. E. Huang, Q. Ma, Z. Liu, Etalon array reconstructive spectrometry. *Sci. Rep.* **7**, 40693 (2017).
11. P. Fan, U. K. Chettiar, L. Cao, F. Afshinmanesh, N. Engheta, M. L. Brongersma, An invisible metal–semiconductor photodetector. *Nat. Photon.* **6**, 380–385 (2012).
12. L. Cao, J.-S. Park, P. Fan, B. Clemens, M. L. Brongersma, Resonant germanium nanoantenna photodetectors. *Nano Lett.* **10**, 1229–1233 (2010).
13. S. Mokkapati, D. Saxena, H. H. Tan, C. Jagadish, Optical design of nanowire absorbers for wavelength selective photodetectors. *Sci. Rep.* **5**, 15339 (2015).
14. O. Hayden, R. Agarwal, C. M. Lieber, Nanoscale avalanche photodiodes for highly sensitive and spatially resolved photon detection. *Nat. Mater.* **5**, 352–356 (2006).
15. Q. Li, J. van de Groep, Y. Wang, P. G. Kik, M. L. Brongersma, Transparent multispectral photodetectors mimicking the human visual system. *Nat. Commun.* **10**, 4982 (2019).
16. A. Tittl, A. Leitis, M. Liu, F. Yesilkoy, D.-Y. Choi, D. N. Neshev, Y. S. Kivshar, H. Altug, Imaging-based molecular barcoding with pixelated dielectric metasurfaces. *Science* **360**, 1105–1109 (2018).
17. X. Zhu, C. Vannahme, E. Højlund-Nielsen, N. A. Mortensen, A. Kristensen, Plasmonic colour laser printing. *Nat. Nano* **11**, 325–329 (2016).
18. X. Zhu, W. Yan, U. Levy, N. A. Mortensen, A. Kristensen, Resonant laser printing of structural colors on high-index dielectric metasurfaces. *Sci. Adv.* **3**, e1602487 (2017).
19. M. W. Knight, H. Sobhani, P. Nordlander, N. J. Halas, Photodetection with active optical antennas. *Science* **332**, 702–704 (2011).
20. A. Sobhani, M. W. Knight, Y. Wang, B. Zheng, N. S. King, L. V. Brown, Z. Fang, P. Nordlander, N. J. Halas, Narrowband photodetection in the near-infrared with a plasmon-induced hot electron device. *Nat. Commun.* **4**, 1643 (2013).
21. B. Y. Zheng, Y. Wang, P. Nordlander, N. J. Halas, Color-selective and CMOS-compatible photodetection based on aluminum plasmonics. *Adv. Mater.* **26**, 6318–6323 (2014).
22. M. Tanzid, A. Ahmadivand, R. Zhang, B. Cerjan, A. Sobhani, S. Yazdi, P. Nordlander, N. J. Halas, Combining plasmonic hot carrier generation with free carrier absorption for high-performance near-infrared silicon-based photodetection. *ACS Photon.* **5**, 3472–3477 (2018).
23. Z. Fang, Z. Liu, Y. Wang, P. M. Ajayan, P. Nordlander, N. J. Halas, Graphene-antenna sandwich photodetector. *Nano Lett.* **12**, 3808–3813 (2012).
24. H. Wang, J. W. Lim, F. M. Mota, Y. J. Jang, M. Yoon, H. Kim, W. Hu, Y.-Y. Noh, D. H. Kim, Plasmon-mediated wavelength-selective enhanced photoresponse in polymer photodetectors. *J. Mater. Chem. C* **5**, 399–407 (2017).
25. B. Desiatov, I. Goykhman, N. Mazurski, J. Shappir, J. B. Khurgin, U. Levy, Plasmonic enhanced silicon pyramids for internal photoemission Schottky detectors in the near-infrared regime. *Optica* **2**, 335–338 (2015).

26. M. Alavirad, L. Roy, P. Berini, Surface plasmon enhanced photodetectors based on internal photoemission. *J. Photonics Energy* **6**, 042511 (2016).
27. X. Yu, Z. Dong, J. K. W. Yang, Q. J. Wang, Room-temperature mid-infrared photodetector in all-carbon graphene nanoribbon-C_{60} hybrid nanostructure. *Optica* **3**, 979–984 (2016).
28. X. Yu, Z. Dong, Y. Liu, T. Liu, J. Tao, Y. Zeng, J. K. W. Yang, Q. J. Wang, A high performance, visible to mid-infrared photodetector based on graphene nanoribbons passivated with HfO_2. *Nanoscale* **8**, 327–332 (2016).
29. J. Bao, M. G. Bawendi, A colloidal quantum dot spectrometer. *Nature* **523**, 67–70 (2015).
30. Ž. Zobenica, R. W. van der Heijden, M. Petruzzella, F. Pagliano, R. Leijssen, T. Xia, L. Midolo, M. Cotrufo, Y. Cho, F. W. M. van Otten, E. Verhagen, A. Fiore, Integrated nano-opto-electro-mechanical sensor for spectrometry and nanometrology. *Nat. Commun.* **8**, 2216 (2017).
31. Z. Wang, S. Yi, A. Chen, M. Zhou, T. S. Luk, A. James, J. Nogan, W. Ross, G. Joe, A. Shahsafi, K. X. Wang, M. A. Kats, Z. Yu, Single-shot on-chip spectral sensors based on photonic crystal slabs. *Nat. Commun.* **10**, 1020 (2019).
32. M. Garín, R. Fenollosa, R. Alcubilla, L. Shi, L. F. Marsal, F. Meseguer, All-silicon spherical-Mie-resonator photodiode with spectral response in the infrared region. *Nat. Commun.* **5**, 3440 (2014).
33. J. J. Cadusch, J. Meng, B. J. Craig, V. R. Shrestha, K. B. Crozier, Visible to long-wave infrared chip-scale spectrometers based on photodetectors with tailored responsivities and multispectral filters. *Nanophotonics* **9**, 3197–3208 (2020).
34. J. S. T. Smalley, X. Ren, J. Y. Lee, W. Ko, W.-J. Joo, H. Park, S. Yang, Y. Wang, C. S. Lee, H. Choo, S. Hwang, X. Zhang, Subwavelength pixelated CMOS color sensors based on anti-hermitian metasurface. *Nat. Commun.* **11**, 3916 (2020).
35. A. I. Kuznetsov, A. E. Miroshnichenko, M. L. Brongersma, Y. S. Kivshar, B. Luk'yanchuk, Optically resonant dielectric nanostructures. *Science* **354**, eaag2472 (2016).
36. W. Yang, S. Xiao, Q. Song, Y. Liu, Y. Wu, S. Wang, J. Yu, J. Han, D.-P. Tsai, All-dielectric metasurface for high-performance structural color. *Nat. Commun.* **11**, 1864 (2020).
37. W. Yang, G. Qu, F. Lai, Y. Liu, Z. Ji, Y. Xu, Q. Song, J. Han, S. Xiao, Dynamic bifunctional metasurfaces for holography and color display. *Adv. Mater.* **33**, 2101258 (2021).
38. Z. Dong, T. Wang, X. Chi, J. Ho, C. Tserkezis, S. L. K. Yap, A. Rusydi, F. Tjiptoharsono, D. Thian, N. A. Mortensen, J. K. W. Yang, Ultraviolet interband plasmonics with Si nanostructures. *Nano Lett.* **19**, 8040–8048 (2019).
39. Z. Dong, L. Jin, S. D. Rezaei, H. Wang, Y. Chen, F. Tjiptoharsono, J. Ho, S. Gorelik, R. J. H. Ng, Q. Ruan, C.-W. Qiu, J. K. W. Yang, Schrödinger's red pixel by quasi-bound-states-in-the-continuum. *Sci. Adv.* **8**, eabm4512 (2022).
40. X. M. Goh, Y. Zheng, S. J. Tan, L. Zhang, K. Kumar, C.-W. Qiu, J. K. W. Yang, Three-dimensional plasmonic stereoscopic prints in full colour. *Nat. Commun.* **5**, 5361 (2014).
41. L. Jiang, T. Yin, Z. Dong, H. Hu, M. Liao, D. Allioux, S. J. Tan, X. M. Goh, X. Li, J. K. W. Yang, Z. Shen, Probing vertical and horizontal plasmonic resonant states in the photoluminescence of gold nanodisks. *ACS Photon* **2**, 1217–1223 (2015).
42. E. D. Palik, *Handbook of Optical Constants of Solids* (Academic Press, 1998).
43. J. H. Ho, C. L. Lee, T. F. Lei, T. S. Chao, Ellipsometry measurement of the complex refractive index and thickness of polysilicon thin films. *J. Opt. Soc. Am. A* **7**, 196–205 (1990).
44. J. Ho, Y. H. Fu, Z. Dong, R. Paniagua-Dominguez, E. H. H. Koay, Y. F. Yu, V. Valuckas, A. I. Kuznetsov, J. K. W. Yang, Highly directive hybrid metal–dielectric Yagi-Uda nanoantennas. *ACS Nano* **12**, 8616–8624 (2018).
45. C. P. Y. Wong, C. Troadec, A. T. S. Wee, K. E. J. Goh, Gaussian thermionic emission model for analysis of Au/MoS_2 Schottky-barrier devices. *Phys. Rev. Applied* **14**, 054027 (2020).
46. S. M. Sze, *Physics of Semiconductor Devices* (Wiley-Interscience, ed. 2, 1981).
47. H. C. Card, Aluminum-silicon Schottky barriers and ohmic contacts in integrated circuits. *IEEE Trans. Electron Devices* **23**, 538–544 (1976).
48. B. J. Park, J. Jung, C.-R. Moon, S. H. Hwang, Y. W. Lee, D. W. Kim, K. H. Paik, J. R. Yoo, D. H. Lee, K. Kim, Deep trench isolation for crosstalk suppression in active pixel sensors with 1.7 μm pixel pitch. *Jpn. J. Appl. Phys.* **46**, 2454–2457 (2007).
49. Z. Dong, S. Gorelik, R. Paniagua-Dominguez, J. Yik, J. Ho, F. Tjiptoharsono, E. Lassalle, S. D. Rezaei, D. C. J. Neo, P. Bai, A. I. Kuznetsov, J. K. W. Yang, Silicon nanoantenna mix arrays for a trifecta of quantum emitter enhancements. *Nano Lett.* **21**, 4853–4860 (2021).
50. E. E. Radescu, G. Vaman, Exact calculation of the angular momentum loss, recoil force, and radiation intensity for an arbitrary source in terms of electric, magnetic, and toroid multipoles. *Phys. Rev. E* **65**, 046609 (2002).
51. Z. Dong, J. Ho, Y. F. Yu, Y. H. Fu, R. Paniagua-Dominguez, S. Wang, A. I. Kuznetsov, J. K. W. Yang, Printing beyond sRGB color gamut by mimicking silicon nanostructures in free-space. *Nano Lett.* **17**, 7620–7628 (2017).
52. C. C. Fesenmaier, Y. Huo, P. B. Catrysse, Optical confinement methods for continued scaling of CMOS image sensor pixels. *Opt. Express* **16**, 20457–20470 (2008).
53. A. D. Monte, Technology development on CMOS image sensors (Lfoundry, 2019); https://indico.cern.ch/event/855527/attachments/1924667/3225909/adelmonte_-_Technology_development_of_CMOS_Image_sensors.pdf.
54. R. Paschotta, RF Photonics Encyclopedia;https://rp-photonics.com/responsivity.html.

Acknowledgments

Funding: This work was supported by A*STAR Career Development Award grant C210112019 (to Z.D.), A*STAR AME IRG grant A20E5c0093 (to J.K.W.Y. and Z.D.), A*STAR SERC Pharos grant 1527300025 (to A.I.K. and J.K.W.Y.), A*STAR MTC Programmatic grant M21J9b0085 (to A.I.K. and J.K.W.Y.), A*STAR MTC IRG grant M21K2c0116 (to Z.D.), A*STAR MTC YIRG grant M21K3c0127 (to Z.D.), A*STAR SERC Pharos grant 1527000016 (to C.P.Y.W.), A*STAR AME YIRG grant A2084c0179 (to C.P.Y.W.), National Research Funding (NRF) Singapore NRF-CRP20-2017-0001 (to J.K.W.Y.), and National Research Funding (NRF) Singapore NRF-NRFI06-2020-0005 (to J.K.W.Y.) **Author contributions:** Conceptualization: J.H., Z.D., and J.K.W.Y. Methodology: J.H., Z.D., and J.K.W.Y. Fabrication: F.T., J.H., Z.D., K.C.H.G., M.W., S.L., and C.P.Y.W. Characterization: H.S.L., J.H., J.Z., Z.D., and J.C. Simulation: J.H., S.D.R., and C.P.Y.W. Discussions and suggestions: A.I.K. and C.P.Y.W. Supervision: Z.D. and J.K.W.Y. Writing—original draft: J.H., Z.D., and J.K.W.Y. Writing—review and editing: Z.D. and J.K.W.Y. All the authors discussed the results and commented on the manuscript. **Competing interests:** The authors declare that they have no competing interests. **Data and materials availability:** All data needed to evaluate the conclusions in the paper are present in the paper and/or the Supplementary Materials. The data that support the plots within this paper and other findings of this study are published on the open access data repository of Zenodo: https://zenodo.org/record/7022700#.Ywg-a3FByUl.

Submitted 8 June 2022
Accepted 25 October 2022
Published 23 November 2022
10.1126/sciadv.add3868